Journal of Applied Research and Technology

www.jart.icat.unam.mx

Journal of Applied Research and Technology 23 (2025) 638-650

Original

TDOCT with Optical Delay Line based on Static Helicoid Mirror

O. Kolokoltsev[1]* • M. Avendaño Alejo[1] • I. Gómez Arista[2]
N. Qureshi[1] • E. Mejia[1]

[1]*Instituto de Ciencias Aplicadas y Tecnología, Universidad Nacional Autónoma de México, CU 04510, Cd. México, México.*
[2]*CONAHCYT-INAOE, Luis Enrique Erro # 1, Tonantzintla, Puebla, Mexico C.P. 72840*

Received: 07 07 2024; Accepted: 03 12 2025
Available: 12 31 2025

Abstract: In this work, we described a design of Optical Delay Line (ODL) for Time Domain Optical Coherence Tomography (TDOCT). ODL is based on a static helicoid mirror, integrated with an optical deflector. The delay line can provide up to 10 mm scanning depth range, thanks to its multi-pass configuration. The TDOCT system has been analyzed and optimized to operate in ultrahigh depth resolution regime. The estimated sensitivity of the TDOCT, at the presence of the relatively high level of the photon excess noise, can be of the order of -94 dB.

Keywords: Optical Coherence Tomography, Optical Delay Line, Helicoid Mirror.

*Corresponding author.
E-mail address: oleg.kolokoltsev@icat.unam.mx (O. Kolokoltsev).
Peer Review under the responsibility of Universidad Nacional Autónoma de México.

Introduction

Optical delay lines (ODL) have been a subject of interest for decades because of their great importance for a variety of time-resolved spectroscopic systems. Depending on the application, ODL must be optimized for the depth scanning range, repetition rate of the depth scanning (A-scan rate), polarization selectivity, dynamic range, dispersion characteristics, etc. Among the early solutions are the piezoelectric stretching of optical fiber coil (Henderson et al., 2004), diffraction grating integrated with a galvo-mirror scanner (Rollins et al., 1998), and polygon rotating mirrors (Delachenal et al., 1999). A very interesting recently proposed solution is ODL based on a rotating helicoid mirror (HM) (Kim et al., 2008). This element was successfully implemented in an optical autocorrelator (Wang et al., 2009), terahertz spectrometer (Molter et al., 2010), and adaptive wave front formation system (Pal et al., 2008). ODL based on HM possesses several advantages: linear periodical scanning speed, minimal dispersion, relatively large delay range. The combination of these characteristics makes a helical mirror ODL very attractive for time domain optical coherence tomography (TDOCT). The axial (or depth) resolution of TDOCT is typically 10–30 μm and is basically determined by the coherence length of a broadband light source. Scanning ODLs for TDOCT have been realized by combining a galvo-mirror scanner with reflective elements, such as a 3D flat-mirror retroreflector (Locharoenrat & Hsu, 2012), a flat-curved mirrors system (Liu et al., 2004), a system of flat mirrors and a lens (Windecker et al., 1997). The most popular ODL is based on a system that includes a galvo-mirror, a lens, and a diffraction grating (Rollins et al., 1998; Zvyagin et al., 2003). The common drawback of these systems is limited scan depth at high A-scan rates and non-linear scanning velocity of a galvo-mirror. These problems can be overcome with the help of HM ODL. In this work, we present a design of ODL with static HM integrated with an optical deflector. A configuration with static HM is more flexible compared to rotary HM (Kim et al., 2008; Wang et al., 2009; Molter et al., 2010) because, as a deflector, one can use a small rotary mirror attached to a motor axis, a dual-axis galvo-mirror, or a fast MEMS mirror. In such a system, the deflector provides stable conical rotation of the optical beam, and the delay varies at a constant velocity. A unique dispersive element in HM ODL is a lens between HM and the deflector. It is expected that this solution can provide ultrahigh depth resolution of TDOCT and, at the same time, fast axial scan without “dead time”.

An OCT system with ultrahigh resolution must be optimized over an ultrawide spectral range, since depth resolution is inversely proportional to the spectral bandwidth of the light source. In early works on ultrahigh depth resolution, W. Drexler and his coauthors (Drexler et al., 1999) have demonstrated 1 μm resolution in biological tissue by using a femtosecond Ti:sapphire laser. The resolution of 2 μm in tissue, obtained with the help of a nonlinear microstructured fiber, has been reported in (Hartl et al., 2001). Then, rapid and successive developments of compact white-light supercontinuum lasers based on photonic crystal fiber (PCF) made this source mainstream for high-resolution OCT (Wang et al., 2003; Lim et al., 2005; Nishizawa & Yamanaka, 2021; Labruyère et al., 2012; Sylvestre et al., 2021; Froehly & Meteau, 2012). Modern market offers supercontinuum optical sources generating ultrawideband spectra, from 400 to more than 2000 nm, at 20-320 MHz repetition rates. Among them are SuperK EVO, Indus Forte, SuperK Extreme (320 MHz), and SC500-FC. Arctic Photonics offers a very compact source with a bandwidth of 750 - 1750 nm at a 20 kHz repetition rate. A microchip solution for the supercontinuum light source has been described in Ref. (Ji et al., 2021).

In this work, we describe a new ODL configuration and analyze two critical parameters, which determine the depth resolution and the penetration depth of a wideband OCT system: the dispersion and the sensitivity. The analysis includes a single and a balanced detector configuration of TDOCT. It is shown that the sensitivity of both configurations can be maximized using optimal reflectivity of HM ODL and an optimal power of a light source.

1. ODL design

A classic TDOCT is based on a Michelson Interferometer (MI) with a dynamic ODL in the reference arm. The block diagram of the system is shown in Fig.1. It consists of a broadband light source, the cube beamsplitter (BS) with operating wavelength range of 1100 - 1600 nm, the photodetector (PD), the two-axis galvo scanner head (GS), in the sample (object) arm, that is integrated with the scan objective (SO), and the A-Scan (or depth scan) module based on HM ODL in the reference arm. The details of the A-scan module are presented in Fig.2 (the result of CAD simulations).

The operation principle of the module is the following. The optical beam, emitted by the source, passes through the lens L, then passes through the hole of the plane ring mirror (PRM),

reflects from the tilt rotary mirror RM, again passes through the lens, and is retroreflected to RM by the helicoid mirror. Then, RM directs this beam to the plane ring mirror that operates as a retroreflector. In the module, such elements as HM, the optical source, and RM are in the lens focal plane. The rotary tilt mirror provides conical beam scanning over the lens surface. It should be noticed that PRM does not perturb the upper rays shown in the figure, and that the direction of the beam reflected from HM differs from the incident beam by a double slope angle of HM. The benefit of the design is that the beam traces shown in Fig.2 are similar at any angle of the motor axis. The parameters of HM in Fig.2 correspond to 5 mm pitch ($\Delta\ell$) of the helicoid mirror. It is worth noting that the motor "M" shown in Fig.1 can be replaced by a dual-axis galvo-mirror, which can provide a circular deflection of the laser beam.

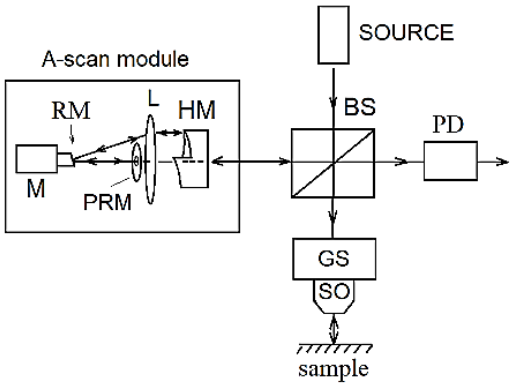

Figure 1. The diagram of the Michelson Interferometer. BS is the cube beamsplitter, PD is the photodetector. In the reference arm: M is the motor that rotates the tilted mirror RM, HM is the helicoid mirror, PRM is the plane ring mirror, L is the lens. In the object arm: GS is the two coordinate galvo scanner with the scan objective (SO).

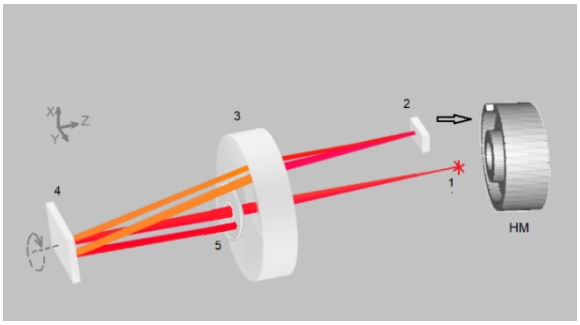

Figure 2. The A-scan module: 1 is the light source, 2 is the reflective segment of the static HM, 3 is the lens with the focus plane at 110 mm, 4 is the rotary tilted mirror (RM), 5 is the plane ring mirror (PRM). The RM tilt angle is 7 degrees. The HM slope angle is 3 degrees, and its diameter is 3 cm.

2. Theoretical Analysis

2.1 Detection algorithm

The BS in the interferometer distributes the optical field of the source between the A-scan module and the object channel. Then, BS combines the optical fields $E_r(t_1)$ and $E_o(t_2)$ reflected from the A-Scan module and the object arm, respectively, and sends them into a photodiode. The optical fields are mixed in the photodiode to give an electrical signal (Tomlins & Wang, 2005):

$$I(\tau) = I_r + I_o + 2Re(\Gamma(\tau)), \quad (1)$$

where, $\tau = t_1 - t_2$ is the delay between the fields, $I_r = \langle E_r E_r^* \rangle$ and $I_0 = \langle E_o E_o^* \rangle$ are the static background signals from the reference and the object arms,

$$\Gamma(\tau) \propto \int \quad E_r(t) E_o^*(t+\tau) dt \quad (2)$$

is the cross-correlation function (or coherence function) that represents the "useful" signal. It describes an envelope filled with a carrier frequency (f_0) that is determined by the scanning period of the A-scan module. The static background signals I_r and I_o can be eliminated by using a balanced photodetector (BPD). The delay τ can be expressed through the optical path length difference (ΔL) between the channels $\tau = \Delta L/c$, where c is the speed of light. In turn, ΔL is modulated with a scanning period (T) by the ODL. It is supposed that $\boldsymbol{\Delta L}$ induced by the HM is a linear function of time, within the period T. Also, $\boldsymbol{\Delta L}$ can be a function of ω because of the dispersion in the ODL optics. Due to the multi-pass configuration of the ODL shown in Fig.2, maximum value of $\boldsymbol{\Delta L} = 2\Delta\ell = 10$ mm.

To extract the waveform envelope as well as to eliminate the phase instability of the waveform, we propose the following numerical quadrature detection algorithm. The real signal $\boldsymbol{I(\tau)}$ is digitized by an acquisition card. Then, by using the Hilbert transform $\boldsymbol{I(\tau)}$ is converted to signals $\boldsymbol{I_{Re}}$ and $\boldsymbol{I_{Im}}$ (shifted by π/2 rad). This operation consists in calculation of the so-called analytical signal (Z) from the spectrum (S) of the signal $\boldsymbol{I(\tau)}$:

$$Z(\tau) = \frac{1}{\pi}\int_0^\infty \quad S(\omega) e^{j\omega} d. \quad (3)$$

The desirable signals are: $\boldsymbol{I_{Re} = Re(Z)}$ and $\boldsymbol{I_{Im} = Im(Z)}$. Here, for the numerical implementation of Eq.3 one can use the real direct and complex inverse fast Fourier transforms, ($\boldsymbol{F}$) and ($\boldsymbol{F^{-1}}$), respectively:

$$Z = F^{-1} * (F * I). \quad (4)$$

Finally, the response of the reflectometer is calculated as $10logc(U_{max}/U)$, where $U = I_{RE}^2 + I_{Im}^2$. An advantage of this algorithm is an insensitivity to the phase fluctuations between $E_r(t_1)$ and $E_o(t_2)$, as well as the possibility to process a signal envelope that contains only one period of the carrier frequency (f_0). The frequency f_0 is the mixing product of the object channel lightwave and the Doppler-shifted reference lightwave: $f_0\ v_p\ /\lambda_c$, where v_p is the velocity of the scanning mirror (HM), determined through the scanning period T, $v_p \approx l/T$ (f_0 = 700 kHz at T = 1 ms, and $\Delta\ell$ = 1 mm). The result of this algorithm is shown in Fig.3.

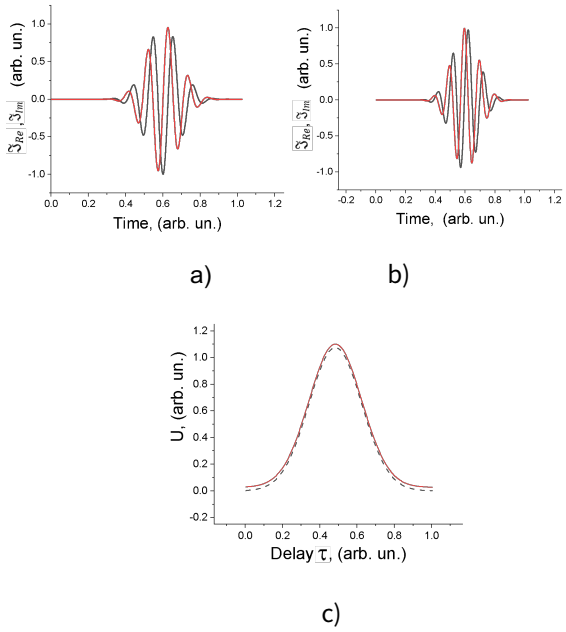

Figure 3. Simulated responses I_{Re} (*black curve*) and I_{Im} (*red curve*) at the different phase states a) and b). The correspondent envelopes of U $\sim|\Gamma(\tau)|^2$ are shown in Fig. c) by dashed and solid curves, respectively.

2.2 Axial Resolution

Theoretical free-space axial resolution of the system, with a mirror in the interferometer object arm, can be estimated by the expression for the round-trip coherence length of an optical source with Gaussian spectrum (Aumann et al., 2019):

$$\delta = \frac{2ln\,(2)}{\pi}\frac{\lambda_c^2}{\Delta\lambda}, \tag{5}$$

where λ_c is the central wavelength of the source, and $\Delta\lambda$ is the full width at half maximum (FWHM) of the spectrum of optical source. The estimated value of the Rayleigh axial resolution of the double-pass system is $\delta_R = \frac{\beta\delta}{2}$, where β is the broadening factor determined by the material dispersion of optical elements.

2.3 Analysis of dispersion effects

Because of the dispersive elements in the interferometer the coherence function can acquire significant distortions if there is mismatch in the group delay between the reference and the sample arms. Dispersion of optical elements in the two interferometer arms must be carefully compensated (Drexler et al., 2015; Hitzenberger et al., 1999; Hitzenberger, 2004). There are two methods of dispersion compensation: real-time physical device and numerical post processing (Smith et al., 2002; Fercher et al., 2002; Choi et al., 2012). Here we consider dispersion in the reference arm only, because dispersion in the object arm depends on optical properties of specific sample (Photiou & Pitris, 2019). In the configuration presented in Fig.2 the dispersive elements are the lens in ODL, the cube beamsplitter, and a scan objective lens in the GS head in the object arm. The commercial scan objective is usually supplied by a corresponding dispersion-compensating block that must be installed in the reference arm. Also, the optical paths inside the beamsplitter are perfectly balanced. Hence, the scan objective and BS can be excluded from the analysis. To reveal the dispersion effects, it is convenient to analyze Eq. (2) in the frequency domain where the phase effects induced by optical elements have an additive effect on the spectral components of the fields (Drexler et al., 2015). This can be done by using the convolution property of Fourier Transform (F):

$$F\{\Gamma\} = F\{E_r\} \cdot F\{E_o^*\}, \tag{6}$$

where: $F\{E_r\} = S(\omega)h_r(\omega)$, $F\{E_o^*\} = (S(\omega)h_o(\omega))^*\ S(\omega)$ is the power spectral density of the light source, $h_o(\omega)$ and $h_r(\omega)$ are complex spectral functions of the fields reflected from the object and reference arms, respectively. The characteristics of the A-Scan module can be analyzed assuming that the sample is a perfect mirror with $h_o(\omega) = 1$, and ODL induces the function $h_r(\omega) = \sqrt{H(\omega)}exp\ (-j\varphi(\omega))$, where $H(\omega)$ is the spectral power and $\varphi(\omega)$ is the spectral phase. These functions are related to the lens in the A-scan module shown in Fig.2. Therefore, the convolution given by Eq. (2) can be re-written as:

$$\Gamma = F^{-1}\{S(\omega) \cdot S^*(\omega)\sqrt{H(\omega)}e^{j\varphi(\omega)}\}. \tag{7}$$

The spectral phase $\varphi(\omega)$ in Eq. (7) can be expanded in a Taylor series:

$$\varphi \approx \varphi_0 + GD\Delta\omega + \frac{1}{2}GDD(\Delta\omega)^2 + \cdots, \tag{8}$$

where $\Delta\omega = \omega_c - \omega$, $\omega_c = 2\pi c/\lambda_c$, $GD = \frac{\partial\varphi}{\partial\omega} = \tau_g$ is the group delay, $GDD = \partial^2\varphi/\partial\omega^2$ is the group delay dispersion (strictly

speaking all these terms also are functions of ω). The interpretation of these terms is the following. *GD* term induces the group delay τ_g of the envelope of Γ(τ), while the *GDD* term can lead to broadening and the chirp of $\Gamma(\tau)$ envelope. Note that in Eq.8 the phase φ = Δ*z*(ω*n*(ω)/c) contains no compensated path difference Δ*z* induced by dispersive optics in the interferometer arms. Also, here, the coherence function that corresponds to dispersionless case is denoted as $\Gamma_0(\tau)$. To evaluate the dispersion effects let us suppose that the spectral density of a broadband source *S*(ω) has a Gaussian shape:

$$S(\omega) = S(\omega_c)exp\left(-4ln(2)\left(\frac{\Delta\omega}{\Delta\omega_{FWHM}}\right)^2\right), \quad (9)$$

where ω_{FWHM} is the FWHM of the spectrum in the frequency domain. The influence of GD and GDD can be calculated by using the Sellmeier equation for the refractive index *n*(ω).

One of the important tasks when developing OCT is to achieve high axial resolution. This requires optical sources with increased bandwidth to decrease the coherence length (δ ~1/Δλ). Therefore, it is interesting to determine a limiting bandwidth of a source at which GDD of optic elements does not cause significant broadening of $\Gamma(\tau)$, as well as to calculate parameters of a dispersion compensator to compensate strong GDD effect. Let us consider the lens in the A-Scan module fabricated of N-BK7 glass, which has zero GDD at λ = 1.322 μm. In the simulations we considered that light passes the lens 6 times, i.e. Δz = 2×s_1 + 4×s_2 mm, where s_1 = 5 mm and s_2 = 4 mm are, respectively, the axial and peripherical thickness of the lens. Also, all simulations here were done for light sources at λc = 1.3 μm. The analysis of Eq.(7) shows, for example, that FWHM of $\Gamma_0(\tau)$ for commercial superluminiscent diode, that emits Δλ = 80 nm centered at λ_c = 1.3 μm, is of 30 fs. In the space domain it is equivalent to the coherence length of δ ≈ 10 μm.

The calculated GD induced by the lens is $\tau_l = 40\ ps$. Although τ_l is comparable to the maximal delay induced by the HM in air $\tau_{HM}\ \frac{l}{c} = 216$ ps, it contributes only to the total delay of $\Gamma(\tau)$ envelope. Since in the free space interferometer this group delay can be easily compensated by the variation of the length of the object arm, this parameter can be excluded from the analysis, as not critical. Here, we pay more attention to GDD. In the case of the considered superluminiscent diode, GDD changes from +154 to -93 fs2 over the spectral range Δλ = 80 nm. Nevertheless, $\Gamma(\tau)$ remains unchanged, i.e. it is practically insensitive to GDD(ω) induced by the lens.

A very weak broadening of $\Gamma(\tau)$ begins at Δλ = 125 nm (Fig.4a). In this case FWHM of $\Gamma_0(\tau)$ = 20 fs, the coherence length is δ = 6 μm, and GDD(ω) changes from +179 to -118 fs2 within Δλ. If a source bandwidth Δλ increases to 250 nm (Fig.4c), GDD(ω) changes from +327 to -266 fs2 within Δλ. In this case GDD transforms the Gaussian $\Gamma_0(\tau)$ with FWHM of 10 fs into asymmetrical function with sidelobes, and the main peak of $\Gamma(\tau)$ broadens by factor β =1.33. This effect becomes more pronounced at Δλ = 356 nm, as seen in Fig.4d, where GDD(ω) changes from +476 to -448 fs2 within Δλ. This case corresponds to FWHM of $\Gamma_0(\tau)$ = 7 fs, and the coherence length δ = 2 μm.

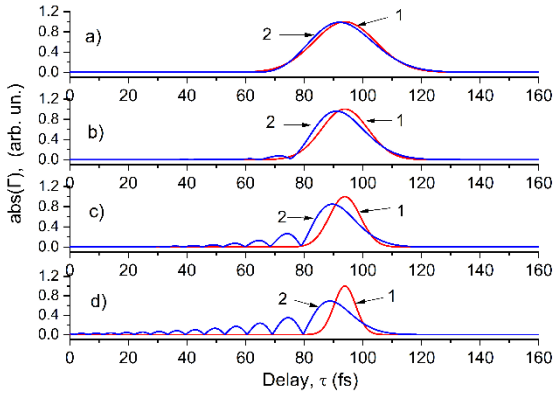

Figure 4. Calculated absolute values of the coherence function. All the curves marked with 1 show $\Gamma_0(\tau)$ in dispersionless case, and the curves marked with "2" show $\Gamma(\tau)$ at GDD ≠0: a) Δλ = 125 nm, b) Δλ = 166 nm, c) Δλ = 250 nm, d) Δλ = 356 nm.

The effect of the material dispersion is explained in Fig.5. In presence of GDD the Gaussian *S*(ω) is transformed into a chirped waveform $Re\left\{S(\omega)\cdot exp(-i\left[2 = \frac{1}{2}GDD(\omega)\cdot(\Delta\omega)^2\right]\right\}$ with a mirror symmetry with respect to ω_c. The spectral bandwidth of this chirped waveform determines the broadening of $\Gamma(\tau)$.

The analysis shows that for the considered system, the coherence function I has a weak sensitivity to GDD if the absolute value of the phase φ2 varies from 0 to less than 10 degrees within FWHM of *S*(ω). In the opposite case, φ2 induces distortion of Γ, as, for example, at Δλ = 250 nm when φ2 changes from +43 to -31 deg.

Obviously, the tradeoff between the axial resolution and the GDD-induced broadening can be resolved with the help of a dispersion compensator. For example, at Δλ = 356 nm GDD of the lens can be compensated by 26 mm thick N-BK7 block, or 20 mm thick fused silica block, installed into the object arm. Fig.6 shows that, at least theoretically, the GDD effect can be

completely compensated, and TDOCT can provide free space resolution of 2 μm (≈1.5 μm in tissue).

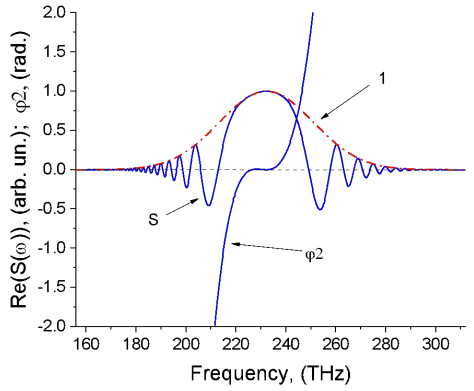

Figure 5. The spectra *S* (ω/2π) and the phase (φ2) induced by GDD at Δ = 250 nm. Curve 1 shows S (ω) at GDD =0.

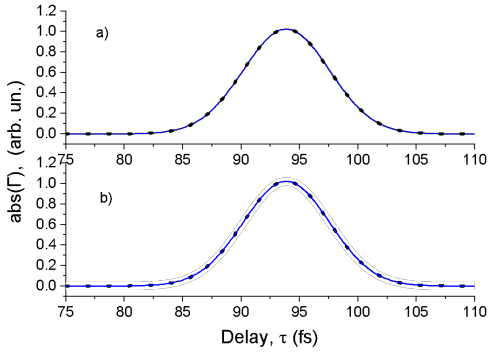

Figure 6. GDD compensation at Δλ = 356 nm. The curves presented by dots and by solid lines show $\Gamma_0(\tau)$ and the compensated $\Gamma(\tau)$, respectively: a) dispersion compensator of 26 mm thick N-BK7 block, b) dispersion compensator of 20 mm thick fused silica block.

Therefore, the A-scan module can be used without the dispersion compensator if the bandwidth of the source does not exceed 120 nm. If the optical source has a wider spectrum, the OCT system must be integrated with a corresponding dispersion compensator.

2.4 Optimization of TDOCT Sensitivity

The sensitivity of OCT is the minimal reflectivity of a sample (R_S) that corresponds to the signal-to-noise ratio (*SNR*) *SNR* = 1. Here, the signal is presented as the mean-square photocurrent of OCT interference signal $\langle I_s^2 \rangle$, and the noise is expressed as the total photocurrent variance (mean-squared current noise) σ^2:

$$SNR = \frac{\langle I_s^2 \rangle}{\sigma^2}. \quad (10)$$

On practice, however, it is more convenient to find a maximum value of *SNR* at $R_S = 1$ (by using a perfect mirror instead of an object) and calculate the minimal R_S by using the relationship (Agrawal et al., 2017):

$$R_S^{min} = \frac{1}{SNR_{max}}. \quad (11)$$

SNR depends on OCT configuration and specific parameters of OCT components. Here we compare two configurations: the system with a single photodetector shown in Fig.1, and the system with the balanced differential photodetection presented in Fig.7.

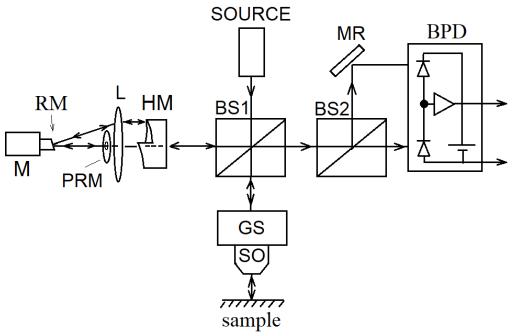

Figure.7. The diagram of the Michelson Interferometer in the differential balanced detection configuration. BPD is the balanced photodetector; MR is the mirror, BS2 is the additional beamsplitter (this element does not introduce disbalance of GDD between the arms).

It was shown (Podoleanu, 2000; Rollins, 1999; Popescu et al., 2011; Takada, 2002) that the advantage of the differential balanced photodetection is the ability to suppress the photon excess noise (σ_{exc}^2) associated with parasitic reflections in OCT system (Takada, 2002) and intensity fluctuations of supercontinuum light sources (Jensen et al., 2019). In some cases, the photon excess noise can exceed the photon shot noise (σ_{sh}^2), which is determined by the photon quantization, and is inherent to all light sources. In our analysis, we consider that σ_{exc}^2 is caused by parasitic reflections in the system. We suppose that the intensity noise of a supercontinuum light source is suppressed by the signal averaging, or the source is designed to operate at the shot noise limit, like all-normal dispersion (ANDi) super-continuum sources (Rao et al., 2021). Therefore, the total noise of the system is

$$\sigma^2 = \sigma_{sh}^2 + \sigma_{exc}^2 + \sigma_r^2, \quad (12)$$

where the receiver noise (σ_r^2) is included. Let us first consider *SNR* for the single detector configuration in Fig.1, which

includes σ_{exc}^2 caused by parasitic reflections from optical interfaces in the object arm (Podoleanu, 2000; Takada, 2002). These reflected waves mix with the reference channel wave in a photodiode, resulting in noise. This occurs because the interacting waves are not correlated due to the large optical path length difference between them.

In Eq.(10) the mean-square photocurrent is $\langle I_s^2 \rangle = 2(\rho P_0)^2 s_p^2 R_r R_s$, where R_r is the reflectivity of the A-scan module in the reference channel, R_s is the reflectivity of a sample, s_p = 0.5 is the split ratio of the beamsplitter, P_0 is the optical power incident from BS to the sample and the reference mirror (HM), $\rho = \frac{q_e \eta}{h\nu_c}$ is the detector responsivity, $_c$ is the center frequency of the source spectrum $S(\omega)$, η is the detector quantum efficiency, h is the Planck constant, q_e is the electron charge. For the configuration considered the noise terms are (Podoleanu, 2000; Jensen et al., 2019; Leitgeb et al., 2003):

$$\sigma_{sh}^2 = 2\rho P_0 (R_r + R_p) s_p B,$$

$$\sigma_{exc}^2 = (1 + \Pi^2)\rho^2 P_0^2 (R_r + R_p)^2 s_p^2 \frac{B}{\Delta\nu_{eff}},$$

where R_p is the parasitic reflectivity in the object arm, which can be caused by the reflections from the optical interfaces, Π is the degree of source light polarization, B is the bandwidth of the receiver electronics, $\Delta\nu_{eff}$ is the effective linewidth of the source. If the source has Gaussian $S(\omega)$:

$$\Delta\nu_{eff} = \sqrt{\frac{\pi}{2ln(2)}} \frac{\Delta\lambda c}{\lambda_c^2}.$$

The noise of a receiver can be presented in the approximation of the thermal (dark) noise of the photodetector which dominates the noise of the circuit:

$$\sigma_r^2 = 4k_B TB/R_{eff},$$

where k_B, T=300 K, and R_{eff} = 1 MΩ, are, respectively, the Boltzmann constant, the temperature, and the effective resistance of the detector. Considering that ρP_0 represents the averaged photoelectron current, $I = \varrho P_0$, the *SNR* for the single detector can be expressed by:

$$SNR_s = = \frac{2I^2 R_r R_s s_p^2}{\left(2qIs_p(R_r + R_p) + \frac{I^2(1+\Pi^2)(R_r+R_p)^2 s_p^2}{\Delta\nu_{eff}} + 4k_B T/R_{eff}\right)B}. \quad (13)$$

SNR of OCT system with the balanced photodetector (in Fig.7) was derived in Ref. (Takada, 2002; Leitgeb et al., 2003):

$$SNR_B = = \frac{2I^2 R_r R_s s_p^2}{\left(2qIs_p(R_r + R_p) + \frac{2I^2(1+\Pi^2) R_r R_p s_p^2}{\Delta\nu_{eff}} + \frac{4k_B T(1-s_p)}{R_{eff}}\right)B}. \quad (14)$$

The photon excess noise in Eq. (14) is presented by the term

$$\tilde{\sigma}_{exc}^2 = \frac{2I^2(1+\Pi^2) R_r R_p s_p^2}{\Delta\nu_{eff}}.$$

It is worth mentioning that in the ideal case the sensitivity of OCT system must be limited by the photon shot noise only:

$$SNR = -10log\left(\frac{P_0 R_S}{h\nu B}\right).$$

Optimization of SNR with respect to the reflectivity of A-scan module.

The simulations for both configurations are shown in Fig. 8,9 in the logarithmic scale $SNR = 10log\left(\frac{\langle I_s^2 \rangle}{\sigma^2}\right)$. The plots show *SNR* as a function of the reflectivity (R_r) of the HM system in the reference arm, chosen as the optimization parameter. The reflectivity of a sample was set to be R_S=1. Also, the figures include the contribution of the noise components separately, calculated as $SNR_i^{noise} = 10log\left(\frac{\langle I_s^2 \rangle}{\sigma_i^2}\right)$. Fig. 8 shows the case of a small parasitic reflectivity R_p = 0.0001, and Fig. 9 shows *SNR* at R_p = 0.04 (normal light incidence). In both figures, the photon excess noise $\tilde{\sigma}_{exc}^2$ for the balanced detection configuration is not included because the values of this term are too large, that makes impossible clear presentation of the other terms. The large values of $\tilde{\sigma}_{exc}^2$ mean that it does not limit the SNR_B, i.e. it is strongly reduced in the balanced detection configuration. This term, as well as the excess noise of the unbalanced configuration, are presented separately in Fig.10, in the negative logarithmic scale $SNR_{Sh} = -10log\left(\frac{\langle I_s^2 \rangle}{\sigma_{Sh}^2}\right)$.

As seen in Fig.8, SNR_S of the single detector configuration has optimal range of the reflectivity $R_r \approx 0.07 \div 0.1$ within which SNR_S maximizes. It is limited by the thermal noise of the detector at small R_r, and by the photon excess noise at large R_r. The maximum of SNR_S is very close to the maximum SNR_B which reaches the fundamental limit determined by the photon shot noise $SNR_B = SNR_{Sh}$ = 92 dB. The minimal sample reflectivity in the balanced and single detector configurations are $R_S^{min} = 6 \times 10^{-10}$, and $R_S^{min} = 8.2 \times 10^{-10}$, respectively. These values were obtained at P_0 =100 μW, B = 100kHz, and $\Delta\upsilon_{eff} = 14.2\ THz\ (\Delta\lambda = 80\ nm)$. When the bandwidth of the receiver electronics is increased to B = 1 MHz, both the SNR_B and SNR_S decrease by 10 dB.

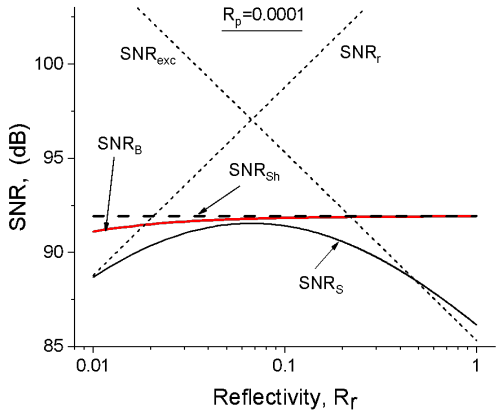

Figure 8. *SNR* as a function of the reflectivity of the A-scan module calculated at R_p = 10-4, R_S =1, B = 100kHz, $\Delta\upsilon_{eff}$ =14.2 THz, Π= 0.7, P_0=100 μW. SNR_{sh}, SNR_{exc}, and SNR_t are the noise sources of the single detector configuration (note $SNR_{Sh}^{single} = SNR_{Sh}^{balanced}$). SNR_S and SNR_B are the functions calculated by Eq. (13) and (14), respectively.

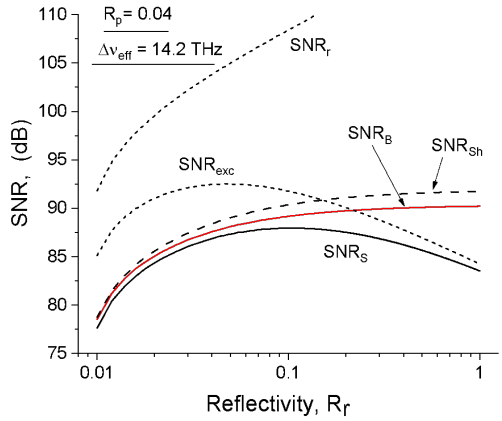

Figure 9. *SNR* as a function of R$_r$, calculated at R_p = 0.04, R_S =1, B = 100kHz, $\Delta\upsilon_{eff}$ =14.2 THz. SNR_{sh}, SNR_{exc}, and SNR_t are the noise sources of the single detector configuration.

The case of high parasitic reflectivity R_p = 0.04 is presented in Fig.9. In this case, SNR_S is limited by the photon shot noise at small R_r, and by the excess noise at $R_r \to 1$. The maximal SNR_S = 88 dB at the optimal R_r = 0.07. SNR_B is mainly limited by the photon shot noise.

It decreases to 90.3 dB, compared to SNR_B in Fig.8, and does not reach the fundamental limit SNR_{Sh}. This occurs because the photon excess noise, in this configuration, increases by 38 dB (Fig.10). Nevertheless, SNR_B exceeds SNR_S.

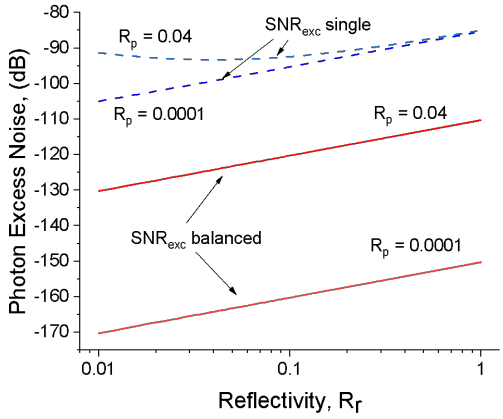

Figure 10. The photon excess noise for the single and balanced detection configurations.

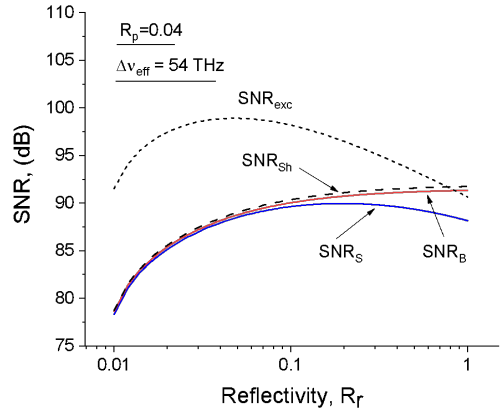

Figure 11. *SNR* calculated at $\Delta\upsilon_{eff}$ = 54 THz, R_p = 0.04, R_S =1, B = 100 kHz. Large $\Delta\upsilon_{eff}$ reduces SNR_{exc}.

Since the excess noise σ_{exc}^2 is inversely proportional to the effective bandwidth $\Delta\upsilon_{eff}$, the contribution of σ_{exc}^2 can be decreased by increasing $\Delta\upsilon_{eff}$. Fig.11 shows that at $\Delta\upsilon_{eff}$ = 54 THz $(\Delta\lambda = 300\ nm)$, the excess noise decreases, and the main limitation factor now is the photon shot noise. As seen in Fig.8,9, and 11, SNR_B maximizes at $R_r \to 1$.

Optimization of SNR with respect to the power P_0.

Optimization of *SNR* with respect to the optical power P_0, at constant reflectivity of the A-scan module, reveals interesting properties of both configurations. The results are presented in Fig.12 and Fig.13.

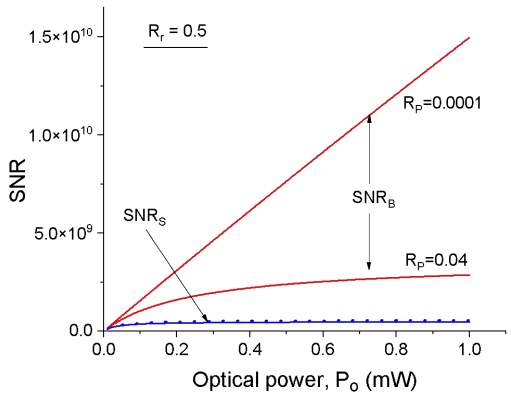

Fig.12. *SNR* as a function of the power P_0, presented by a linear scale. SNR_S (shown by solid and dot curves) at R_p=0.0001 and R_p =0.04 is practically unchanged. However, SNR_B increases by a linear law, at a small parasitic reflectivity R_p. The parameters in the simulation were the following: R_r = 0.5, R_S =1, B = 100 kHz, $\Delta\upsilon_{eff}$ =14.2 THz.

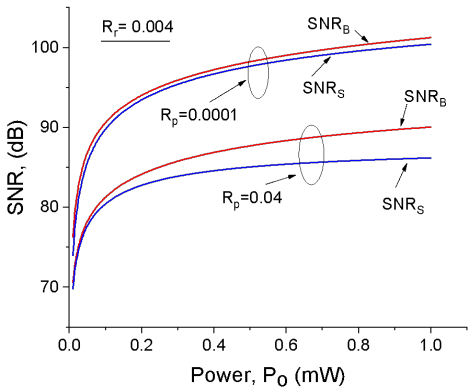

Fig.13. *SNR* as a function of the power P_0. SNR_S curves shown by solid and dot curves coincide at R_p=0.0001 and R_p =0.04. The parameters in the simulation were the following: R_r = 0.004, R_s =1, B = 100 kHz, $\Delta\upsilon_{eff}$ =14.2 THz.

As seen in Fig.12, at relatively high reflectivity of the A-scan module R_r = 0.5, and at small parasitic signal (R_p = 0.0001), SNR_B increases by a linear law, as P_0 increases. At P_0=1 mW SNR_B becomes 10dB of magnitude larger than SNR_S. In turn, SNR_S saturates when P_0 reaches 100 μW. This occurs because SNR_S is limited by the excess noise SNR_{exc} ($SNR_{exc}(P_0) = const$). SNR_B is limited by the shot noise only. Sensitivity of the balanced detection configuration reaches $R_S^{min} = 6.6 \times 10^{-11}$ (SNR_B = 102 dB), and sensitivity of the single detector configuration is $R_S^{min} = 2 \times 10^{-9}$. At large parasitic signal R_p = 0.04, the sensitivity of the balanced configuration decreases to $R_S^{min} = 3.5 \times 10^{-10}$, since the excess noise increases, however SNR_S remains unchanged.

The analysis has shown that there is the range of the reflectivity of the A-scan module, R_r = 0.003÷0.007, which leads to the situation when both SNR_S, and SNR_B have close values over the total range of P_0. This result is shown in Fig.13. Both configurations provide sufficiently low value of the sample reflectivity $R_S^{min} = 7.3 \times 10^{-11}$ (*SNR* =101 dB). This result becomes possible when the parasitic reflectivity is small. Large R_p = 0.04 decreases maximal SNR_B to 90 dB, and SNR_S to 86 dB.

The conclusions from the results shown in section 6 are the following. The optimal reflectivity of ODL for the balanced detector configuration is $R_r \geq 0.5$, and its sensitivity is proportional to the source power (P_0). In contrast, optimal R_r for the single detection configuration is $R_r < 0.1$, and its sensitivity saturates at $P_0 \approx$ 100÷300 μW, depending on R_r.

3. Realization of HM-ODL

The rotation speed of commercial motors (Celeroton AG), which can be used for the rotary tilt mirror, ranges from 100000 rpm (1.6 KHz) to 500000 rpm (8.3 KHz). For real time OCT one axial scan takes 0.08 ms at 512 axial points (a typical 1mm scan depth). This requires at least 500000 rpm motor, which can provide 23 fps. Also, 250000 rpm can be used if HM has two pitches. A motor can be replaced by a 8 -12 KHz XY resonant galvo-mirror scanner, available in the market, or by resonant MEMS mirrors operating at 5-10 KHz.

4. Discussion

As we have shown here, only one element like a lens can limit the depth resolution, and its dispersion must be carefully compensated. The disadvantage of the A-scan module shown in Fig.2 is that the light passes through the lens 6 times. Because of this the calculated dispersion compensator is 20-26 mm thick. The important point is that the compensator must be fabricated from the material that has GDD like GDD of the lens. For example, a prism compensator fabricated from N-SF11 cannot compensate GDD of the lens fabricated from N-BK7. This is the peculiarity of GDD compensation within the ultrawide spectral range. For example, the dispersion of ocular media is compensated by using 25 mm of water in the reference arm.

In principle, the delay line can be designed without a lens, as shown in Fig. 14. This configuration is the simplest ever-presented absolutely dispersionless delay line.

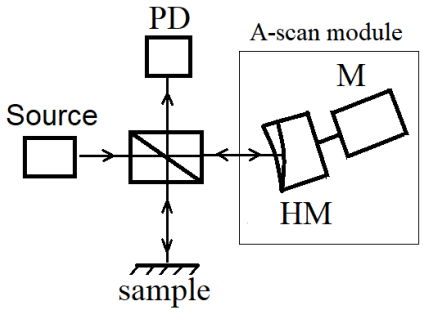

Figure14. The diagram of the Michelson Interferometer with dispersionless A-scan module. The angle between the motor axis and the optical beam incident on HM is equal to the slope angle of HM.

The drawback of this solution is that HM is a relatively heavy asymmetrical metal piece, up to 5 cm in diameter, which will generate a "dangerous" level of mechanical vibrations at ultra-high rotation speeds. The vibration noise itself is not a problem because TD-OCT is a Doppler system, and this noise can be easily filtered. The problem here is mechanical damage of a compact motor.

There is another point to be discussed. In the simulations of the coherence function we used a hypothetical source withλ_c = 1.3 μm and Δλ = 356 nm. With these parameters, when GDD is compensated, we obtained the coherence length δ = 2 μm, by using Eq. (7) (the same result, also, gives Eq. (5)). It is evident, since δ ≈ 1.5λ_c the depth resolution of 2 μm is close to the limit which can be obtained at λ_c = 1.3 μm. Therefore, to get higher resolution one must use a light source with smaller λ_c (Drexler et al., 2015). However, smaller λ_c has lower penetration depth in nontransparent tissue.

The analysis of the noise factors has shown that the photon excess noise, arising from the parasitic reflections, significantly limits the sensitivity of OCT based on the single detector configuration. This noise can be significantly reduced by avoiding normal incidence of light on optic interfaces in the sample arm. At this condition, SNR_S of the interferometer can be optimized and approached to the shot-noise limit (Fig.8). Also, a large effective bandwidth of a source $\boldsymbol{\Delta\upsilon_{eff}}$ is favorable factor that reduces $\boldsymbol{\sigma^2_{exc}}$ (Fig.11).

SNR_B of the balanced detection configuration exceeds SNR_S by 2-10 dB, depending on the optimization parameters. The optimal reflectivity of the A-scan module for TDOCT with the balanced detector is R_r ≈1. As seen in Fig.10, the advantage of the balanced configuration over the single detector configuration with respect to SNR_{exc} is 60 dB at R_p = 0.0001, and 30 dB at R_p = 0.04. For this reason, the sensitivity of the balanced detection configuration is less affected by the excess noise, compared to SNR. SNR_B reaches 102 dB at R_p = 0.0001, and decreases to 94 dB when R_p = 0.04 (P_0=1mW, B = 100KHz).

The calculation of SNR as a function of the optical power P_0 revealed the following: 1) The sensitivity of both configurations increases, as P_0 increases, at a small reflectivity of the A-scan module (Fig.13, R_r ≈0.004). 2) At R_r ≈0.5 the sensitivity of the balanced detection configuration increases, as P_0 increases. However, the sensitivity of the single detector configuration increases only within the power range 0 < P_0<100 μW and remains constant when P_0 > 100 μW (Fig.12). We suppose that this result reflects the fact that the optimal reflectivity R_r of the single detector configuration is R_r ≤ 0.1.

It should be stressed that there is a tradeoff between A-scan rate (which determines the bandwidth B) and sensitivity. For example, some commercial Spectral Domain OCT systems have sensitivity 110 dB at 5.5 kHz of A-scan rate, 96 dB at 75 KHz, and 86 dB at 240 KHz. To compare SNR_B with these parameters we calculated SNR_B at high excess noise (R_p = 0.04), Δλ = 350 nm, and considering that real reflectivity R_r can be ≈ 0.5 (because of the multiple reflections in the A-scan module). The results are the following: 110 dB at B=5.5 KHz, 99.6 dB at B =75 KHz, and 94.6 dB at B =240 KHz. Therefore, the theoretical sensitivity of the TDOCT with the proposed A-scan module is acceptable. The optimal parameters of both configurations are summarized in Table 1.

Table 1. Optimal parameters for the single and balanced OCT configurations, at B=100 kHz and parasitic reflection $R_p = 10^{-4}$ and 0.04.

	Single		Balanced	
	$R_p=10^{-4}$	R_p=0.04	$R_p=10^{-4}$	R_p=0.04
Reflectivity R_r	0.07	0.07	0.1-1	0.1-1
Photon excess noise (dB)	-100	-95	-160	-120
SNR (dB)	92	88	102	94.5
Source power (mW)	0.1		1	

Conclusion

In conclusion, the presented in Fig.2 ODL, based on static helicoid mirror, can provide up to 10 mm scanning depth range, thanks to its multi-pass configuration. On the other hand, the multi-pass configuration requires a relatively thick dispersion compensation element, to use the ODL in ultrahigh depth resolution regime. The sensitivity of the TDOCT system in the single detector configuration is comparable to the sensitivity of the balanced detection configuration, when the excess noise caused by the parasitic reflectivity (R_p) is negligibly small. In this case, SNR_S is maximized at a small reflectivity of the reference channel, $R_r \approx 0.08$. If the parasitic reflectivity is large (R_p=0.04), the sensitivity of the balanced configuration ($\boldsymbol{R_S^{min} = 3.5 \times 10^{-10}}$) is ≈8 dB of magnitude higher than the sensitivity of the single detector configuration. The optimal reflectivity of the reference channel for the balanced detection configuration is $R_r \geq 0.5$, and its sensitivity is proportional to the light source power. Therefore, to minimize the effect of the photon excess noise, TDOCT system must be designed in a balanced detection configuration. An optical source with ultra-wide spectrum also contributes to the minimization of $\boldsymbol{\sigma_{exc}^2}$.

Funding

This work was supported by UNAM PAPIIT grant IT101124.

References

Agrawal, A., Pfefer, T. J., Woolliams, P. D., Tomlins, P. H., & Nehmetallah, G. (2017). Methods to assess sensitivity of optical coherence tomography systems. *Biomedical optics express*, *8*(2), 902-917.
https://doi.org/10.1364/BOE.8.000902

Aumann, S., Donner, S., Fischer, J., & Müller, F. (2019). Optical coherence tomography (OCT): principle and technical realization. *High resolution imaging in microscopy and ophthalmology: new frontiers in biomedical optics*, 59-85.
https://doi.org/10.1007/978-3-030-16638-0_3

Choi, W., Baumann, B., Swanson, E. A., & Fujimoto, J. G. (2012). Extracting and compensating dispersion mismatch in ultrahigh-resolution Fourier domain OCT imaging of the retina. *Optics express*, *20*(23), 25357-25368.
https://doi.org/10.1364/OE.20.025357

Delachenal, N., Wälti, R., Gianotti, R., Christov, S., Wagner, P., Salathe, R. P., ... & Ulbers, G. (1999). Robust and rapid optical low-coherence reflectometer using a polygon mirror. *Optics communications*, *162*(4-6), 195-199.
https://doi.org/10.1016/S0030-4018(99)00093-0

Drexler, W., Chen, Y., Aguirre, A.D., Považay, B., Unterhuber, A., Fujimoto, J.G. (2015). Ultrahigh Resolution Optical Coherence Tomography. *In: Drexler, W., Fujimoto, J. (eds) Optical Coherence Tomography. Springer, Cham.*
https://doi.org/10.1007/978-3-319-06419-2_10

Drexler, W., Morgner, U., Kärtner, F. X., Pitris, C., Boppart, S. A., Li, X. D., ... & Fujimoto, J. G. (1999). In vivo ultrahigh-resolution optical coherence tomography. *Optics letters*, *24*(17), 1221-1223.
https://doi.org/10.1364/OL.24.001221

Fercher, A. F., Hitzenberger, C. K., Sticker, M., Zawadzki, R., Karamata, B., & Lasser, T. (2002). Dispersion compensation for optical coherence tomography depth-scan signals by a numerical technique. *Optics Communications*, *204*(1-6), 67-74.
https://doi.org/10.1016/S0030-4018(02)01137-9

Froehly, L., & Meteau, J. (2012). Supercontinuum sources in optical coherence tomography: a state of the art and the application to scan-free time domain correlation techniques and depth dependant dispersion compensation. *Optical Fiber Technology*, *18*(5), 411-419.
https://doi.org/10.1016/j.yofte.2012.08.001

Hartl, I., Li, X. D., Chudoba, C., Ghanta, R. K., Ko, T. H., Fujimoto, J. G., ... & Windeler, R. S. (2001). Ultrahigh-resolution optical coherence tomography using continuum generation in an air–silica microstructure optical fiber. *Optics letters*, *26*(9), 608-610.
https://doi.org/10.1364/OL.26.000608

Henderson, D.A., Hoffman, C., Culhane, R., & Viggiano III, D. (2004). Kilohertz scanning all-fiber optical delay line using piezoelectric actuation. *Proc. SPIE 5589, Fiber Optic Sensor Technology and Applications* III, 1-8.
http://doi.org/10.1117/12.571572

Hitzenberger, C. K., Baumgartner, A., Drexler, W., & Fercher, A. F. (1999). Dispersion effects in partial coherence interferometry: implications for intraocular ranging. *Journal of Biomedical Optics*, *4*(1), 144-151.
https://doi.org/10.1117/1.429900

Hitzenberger, C.K. (2004). Absorption and Dispersion in OCT. *In: Tuchin, V.V. (eds) Handbook of Coherent Domain Optical Methods. Springer, New York, NY.*
https://doi.org/10.1007/0-387-29989-0_15

Jensen, M., Gonzalo, I. B., Engelsholm, R. D., Maria, M., Israelsen, N. M., Podoleanu, A., & Bang, O. (2019). Noise of supercontinuum sources in spectral domain optical

coherence tomography. *Journal of the Optical Society of America B*, *36*(2), A154-A160.
https://doi.org/10.1364/JOSAB.36.00A154

Ji, X., Mojahed, D., Okawachi, Y., Gaeta, A. L., Hendon, C. P., & Lipson, M. (2021). Millimeter-scale chip–based supercontinuum generation for optical coherence tomography. *Science Advances*, *7*(38), eabg8869.
https://doi.org/10.1126/sciadv.abg8869

Kim, G. J., Jeon, S. G., Kim, J. I., & Jin, Y. S. (2008). High speed scanning of terahertz pulse by a rotary optical delay line. *Review of Scientific Instruments*, *79*(10).
https://doi.org/10.1063/1.2995763

Labruyère, A., Tonello, A., Couderc, V., Huss, G., & Leproux, P. (2012). Compact supercontinuum sources and their biomedical applications. *Optical Fiber Technology*, *18*(5), 375-378.
https://doi.org/10.1016/j.yofte.2012.08.003

Leitgeb, R., Hitzenberger, C. K., & Fercher, A. F. (2003). Performance of fourier domain vs. time domain optical coherence tomography. *Optics express*, *11*(8), 889-894.
https://doi.org/10.1364/oe.11.000889

Lim, H., Jiang, Y., Wang, Y., Huang, Y. C., Chen, Z., & Wise, F. W. (2005). Ultrahigh-resolution optical coherence tomography with a fiber laser source at 1 μ m. *Optics letters*, *30*(10), 1171-1173.
https://doi.org/10.1364/ol.30.001171

Liu, X., Cobb, M. J., & Li, X. (2004). Rapid scanning all-reflective optical delay line for real-time optical coherence tomography. *Optics letters*, *29*(1), 80-82.
https://doi.org/10.1364/OL.30.001744

Locharoenrat, K., & Hsu, I.-J. (2012). Optical Delay Line for Rapid Scanning Low-Coherence Reflectometer. *International Journal of Information and Electronics Engineering*, 2(6), 904-906.
https://ijiee.org/index.php/ijiee/article/view/503

Molter, D., Ellrich, F., Weinland, T., George, S., Goiran, M., Keilmann, F., ... & Léotin, J. (2010). High-speed terahertz time-domain spectroscopy of cyclotron resonance in pulsed magnetic field. *Optics express*, *18*(25), 26163-26168.
https://doi.org/10.1364/OE.18.026163

Nishizawa, N., & Yamanaka, M. (2021). OCT: Ultrahigh resolution optical coherence tomography at visible to near-infrared wavelength region. In *Multidisciplinary Computational Anatomy: Toward Integration of Artificial Intelligence with MCA-based Medicine* (pp. 305-313). Singapore: Springer Singapore.
https://doi.org/10.1007/978-981-16-4325-5_41

Pal Ghai, D., Senthilkumaran, P., & Sirohi, R. S. (2008). Adaptive helical mirror for generation of optical phase singularity. *Applied optics*, *47*(10), 1378-1383.
https://doi.org/10.1364/AO.47.001378

Photiou, C., & Pitris, C. (2019). Comparison of tissue dispersion measurement techniques based on optical coherence tomography. *Journal of biomedical optics*, *24*(4), 046003-046003.
https://doi.org/10.1117/1.JBO.24.4.046003

Podoleanu, A. G. (2000). Unbalanced versus balanced operation in an optical coherence tomography system. *Applied Optics*, *39*(1), 173-182.
https://doi.org/10.1364/AO.39.000173

Popescu, D. P., Choo-Smith, L. P. I., Flueraru, C., Mao, Y., Chang, S., Disano, J., ... & Sowa, M. G. (2011). Optical coherence tomography: fundamental principles, instrumental designs and biomedical applications. *Biophysical reviews*, *3*(3), 155-169.
https://doi.org/10.1007/s12551-011-0054-7

Rao DS, S., Jensen, M., Grüner-Nielsen, L., Olsen, J. T., Heiduschka, P., Kemper, B., ... & Bang, O. (2021). Shot-noise limited, supercontinuum-based optical coherence tomography. *Light: Science & Applications*, *10*(1), 133.
https://doi.org/10.1038/s41377-021-00574-x

Rollins, A. M., & Izatt, J. A. (1999). Optimal interferometer designs for optical coherence tomography. *Optics letters*, *24*(21), 1484-1486.
https://doi.org/10.1364/OL.24.001484

Rollins, A. M., Kulkarni, M. D., Yazdanfar, S., Ung-Arunyawee, R., & Izatt, J. A. (1998). In vivo video rate optical coherence tomography. *Optics express*, *3*(6), 219-229.
https://doi.org/10.1364/OE.3.000219

Smith, E. D., Zvyagin, A. V., & Sampson, D. D. (2002). Real-time dispersion compensation in scanning interferometry. *Optics Letters*, *27*(22), 1998-2000.
https://doi.org/10.1364/ol.27.001998

Sylvestre, T., Genier, E., Ghosh, A. N., Bowen, P., Genty, G., Troles, J., ... & Dudley, J. M. (2021). Recent advances in supercontinuum generation in specialty optical fibers. *Journal of the Optical Society of America B*, *38*(12), F90-F103. https://doi.org/10.1364/JOSAB.439330.

Takada, K. (2002). Noise in optical low-coherence reflectometry. *IEEE Journal of Quantum Electronics*, *34*(7), 1098-1108. https://doi.org/10.1109/3.687850

Tomlins, P. H., & Wang, R. K. (2005). Theory, developments and applications of optical coherence tomography. *Journal of Physics D: Applied Physics*, *38*(15), 2519. https://doi.org/10.1088/0022-3727/38/15/002

Wang, Y., Wang, C., Xing, Q., Liu, F., Li, Y., Chai, L., ... & Zhang, X. (2009). Periodic optical delay line based on a tilted parabolic generatrix helicoid reflective mirror. *Applied optics*, *48*(11), 1998-2005. https://doi.org/10.1364/ao.48.001998

Wang, Y., Zhao, Y., Nelson, J. S., Chen, Z., & Windeler, R. S. (2003). Ultrahigh-resolution optical coherence tomography by broadband continuum generation from a photonic crystal fiber. *Optics letters*, *28*(3), 182-184. https://doi.org/10.1364/OL.28.000182

Windecker, R., Fleischer, M., Franze, B., & Tiziani, H. J. (1997). Two methods for fast coherence tomography and topometry. *Journal of Modern Optics*, *44*(5), 967-977. https://doi.org/10.1080/09500349708230710

Zvyagin, A. V., Smith, E. D., & Sampson, D. D. (2003). Delay and dispersion characteristics of a frequency-domain optical delay line for scanning interferometry. *Journal of the Optical Society of America A*, *20*(2), 333-341. https://doi.org/10.1364/JOSAA.20.000333